Spin-dynamics simulations of the three-dimensional XY model: Structure factor and transport properties

M. Krech
Institut für Theoretische Physik, RWTH Aachen, D-52056 Aachen, Germany

D. P. Landau
Center for Simulational Physics, University of Georgia, Athens, Georgia 30602

(Received 8 December 1998; revised manuscript received 3 March 1999)

We present extensive Monte Carlo spin-dynamics simulations of the classical XY model in three dimensions on a simple cubic lattice with periodic boundary conditions. A recently developed efficient integration algorithm for the equations of motion is used, which allows a substantial improvement of statistics and large integration times. We find spin-wave peaks in a wide range around the critical point and spin diffusion for all temperatures. At the critical point we find evidence for a violation of dynamic scaling in the sense that independent components of the dynamic structure factor $S(\mathbf{q},\omega)$ require different dynamic exponents in order to obtain scaling. Below the critical point we investigate the dispersion relation of the spin waves and the linewidths of $S(\mathbf{q},\omega)$ and find agreement with mode coupling theory. Apart from strong spin-wave peaks we observe additional peaks in $S(\mathbf{q},\omega)$ which can be attributed to two-spin-wave interactions. The overall line shapes are also discussed and compared to mode coupling predictions. Finally, we present results for the transport coefficient $D(q,\omega)$ of the out-of-plane magnetization component at the critical point, which is related to the thermal conductivity of ^{4}He near the superfluid-normal transition. [S0163-1829(99)06629-1]

I. INTRODUCTION

The theoretical investigation of classical spin systems has played a key role in the understanding of phase transitions, critical behavior, scaling, and universality.[1,2] In particular, the classical Ising, the XY, and the Heisenberg model are the most relevant spin models in three dimensions. Each of these simple models represents a universality class which, apart from the spatial dimensionality and the range of the interactions, is characterized by the number of components N of the order parameter, e.g., the magnetization in the case of ferromagnetic models. Despite their simplicity these spin systems continue to be of high relevance within the framework of *dynamic* behavior near critical points[3] (see also Ref. 4 for a recent review). The Ising ($N=1$), the XY ($N=2$), and the Heisenberg ($N=3$) universality class can be extended towards *dynamic* universality classes, which in addition to their static properties are characterized by the set of conservation laws.[3] Special attention must be paid to the presence of energy conserving driving terms in the equations of motion which lead to propagating modes (spin waves) below the critical temperature and thus modify the dynamics.[3] The discrete nature of Ising spins does not allow such terms so that its dynamics is always of relaxational type (see Ref. 3 for a complete classification).

The simplest spin model which allows propagating modes is a particular version of the ferromagnetic XY model ($N=2$). The dynamics here is characterized by a nonconserved order parameter which is dynamically coupled to a *conserved* quantity (see Sec. II). The presence of spin waves reduces the value of the dynamic critical exponent z as compared to pure critical relaxation.[3] The same is true for the isotropic Heisenberg model for which the $N=3$ component magnetization vector is always conserved in the presence of energy conserving driving terms. If the model is ferromagnetic, the magnetization is the order parameter. However, for an *antiferromagnet*, the magnetization plays the role of a conserved vector which is dynamically coupled to the *nonconserved* order parameter (staggered magnetization). This difference in the conservation laws causes the classical Heisenberg ferro- and antiferromagnet to be in different dynamic universality classes although they belong to the same static universality class. Due to their fundamental role in the understanding of the critical dynamics in magnets Heisenberg ferromagnets and antiferromagnets have been thoroughly studied analytically by mode coupling theories (see Ref. 5 for a general overview) especially in the presence of dipolar interactions[6] and numerically by spin dynamics in $d=2$ (Ref. 7) and in $d=3$ (Refs. 8,9) and by methods closely related to molecular dynamics.[10]

The XY model may be viewed as a Heisenberg ferromagnet with an easy-plane (xy) anisotropy such that the order parameter has only two components. Planar ferromagnets are realized by layered compounds such as K_2CuF_4 (Ref. 11) and Rb_2CrCl_4 (Ref. 12) which almost act as two-dimensional systems. The best results available today have been obtained on $CoCl_2$ intercalated in graphite,[13] where a crossover from two-dimensional to three-dimensional behavior in the correlations has been observed below the Kosterlitz-Thouless temperature. Apart from the evident interpretation as a planar ferromagnet the XY model captures a larger variety of phenomena than the Ising or the Heisenberg model. Despite its continuous $O(2)$ symmetry the XY model undergoes a continuous phase transition at a finite temperature in two dimensions, known as the Kosterlitz-Thouless transition.[14] Rather than by the onset of long-ranged order the transition is solely characterized by a diverging correlation length, when the critical temperature is approached from above. Due to a pe-

culiar conspiracy between the spatial dimensionality $d=2$ and the number of spin components $N=2$ configurations of bound and free vortices dominate the critical behavior of the XY model, where the unbinding of vortex pairs marks the point of the phase transition.[14] Naturally, many attempts to describe the critical dynamics of the XY model in $d=2$ theoretically are based on the dynamics of vortices and vortex pairs.[15–18] According to analytical and numerical investigations for the ferromagnetic case[16–19] the in-plane component $S_{xx}(\mathbf{q},\omega)$ and the out-of-plane component $S_{zz}(\mathbf{q},\omega)$ of the dynamic structure factor are expected to have central peaks above the transition. The line shapes of these peaks are predicted to be squared Lorentzian and Gaussian, respectively. Below the transition only spin-wave peaks are expected.[16] To test these specific predictions much numerical effort has been spent on spin dynamics simulations of the XY model in $d=2$.[20,21] Although dynamic finite-size scaling and the value of the dynamical exponent $z=1$ has been confirmed to a high degree of confidence,[20] the measured line shapes of $S(\mathbf{q},\omega)$ (Refs. 20,21) are apparently not well captured by analytical theories (see Ref. 4 for details). It is therefore instructive to measure $S(\mathbf{q},\omega)$ for the XY model in $d=3$ for which configurations of bound or free vortices do not play any special role for the critical behavior and should therefore not provide particularly noticeable contributions to the structure factor. In $d=3$ the dynamics of the planar ferromagnet has been investigated by mode coupling theory[22] and specific predictions concerning line shapes and linewidths have been made which can be compared with our data (see Sec. IV).

It is well known that the λ transition of ^{4}He is in the XY universality class, but the applications of the XY model for the physics of ^{4}He reach far beyond that. The spin dynamics for the XY model is the lattice analog of the dynamical model E (symmetric planar ferromagnet[3]) which *asymptotically* also describes the *critical dynamics* of ^{4}He near the λ line.[3,23–25] If one therefore studies the transport properties of the XY model near the critical point T_c, one should obtain lattice analogs of the corresponding transport coefficients of ^{4}He near the λ transition. In this respect the aforementioned conserved quantity plays a particularly interesting part, because it is related to the entropy density in ^{4}He and its associated transport coefficient corresponds to the thermal conductivity of ^{4}He (Refs. 23,25) which is an experimentally accessible quantity.[26] Below the critical temperature spin waves in the XY model then correspond to travelling waves of second sound in ^{4}He. These propagating modes cause the thermal conductivity to diverge at the lambda transition of bulk ^{4}He.[23,25] In a finite system such as our simulation sample, one therefore expects critical finite-size rounding of the thermal conductivity, which can be studied in the framework of the spin-dynamics simulation and which should also be observable in experiments.

To what extent the spin-dynamics simulation actually captures the critical dynamics of ^{4}He is a rather delicate question. Although the *asymptotic* behavior is described by model E, the actual *crossover* to the asymptotic behavior, i.e., the decay of *nonasymptotic* corrections is governed by the specific heat exponent $\alpha\simeq -0.013$,[27] which is so small that the true asymptotic behavior will never be seen in a simulation. From the point of view of analytic theory this means that in order to capture the nonansymptotic effects present in experiments one has to replace model E by the more complicated model F.[3,23,25,28] From the point of view of spin dynamics simulations this means that one has to look for sources of such nonasymptotic behavior artificially generated by the simulation method and other nonasymptotic corrections not captured by the model or the method (see Sec. II). Apart from these problems, it should also be mentioned that the dynamical model E has two renormalization group fixed points. One of these fixed points yields dynamic scaling with a single dynamic exponent $z=d/2$ in d dimensions, whereas the other gives rise to a weak *violation* of dynamic scaling. Theoretical arguments[24,25,28] and experimental evidence indicate that the latter fixed point is the stable one for ^{4}He in $d=3$, i.e., the critical dynamics is characterized by two different dynamic exponents z_ϕ (order parameter) and z_m (conserved quantity) which fulfill the scaling relation $z_\phi+z_m=d$. Their difference $\omega_w\equiv z_\phi-z_m\neq 0$ has the nature of a dynamic Wegner exponent and is known as the *transient* exponent.[25,28]

The remainder of the paper is organized as follows. In Sec. II we present the model and the simulation methods used to generate equilibrium configurations and to obtain the critical point of the model and its static critical exponents. Furthermore, the equations of motion and the method used to integrate them numerically are presented. In Sec. III we briefly discuss the static critical behavior of our model and present an accurate estimate of the critical temperature. Section IV is devoted to the discussion of the dynamic structure factor and the comparison with predictions of analytic theory. In Sec. V we present results for the lattice analog of the thermal conductivity and discuss its scaling properties. A summary and prospects for future work are given in Sec. VI. Unless otherwise stated statistical errors quoted in this work correspond to one standard deviation.

II. MODEL AND SIMULATION METHOD

The system under investigation is given by a ferromagnetic Heisenberg model with the strongest possible easy-plane anisotropy. The model Hamiltonian reads

$$\mathcal{H}=-J\sum_{\langle ij\rangle}(S_i^xS_j^x+S_i^yS_j^y), \tag{2.1}$$

where $\langle ij\rangle$ denotes a nearest neighbor pair of spins on a simple cubic lattice in three dimensions. The lattice contains L lattice sites in each direction and in order to avoid surface effects periodic boundary conditions are applied. Each spin $\mathbf{S}_i$ is a classical spin $\mathbf{S}_i=(S_i^x,S_i^y,S_i^z)$ with the normalization $|\mathbf{S}_i|=1$. The easy-plane anisotropy in Eq. (2.1) is the strongest possible in the sense that the z components of the spins do not couple, so that Eq. (2.1) looks similar to the standard Hamiltonian for the usual (plane rotator) XY model.

As a starting point for the spin dynamics a sequence of equilibrium configurations is needed to provide initial conditions for the equations of motion. These configurations are obtained from a Monte Carlo simulation of the model Hamiltonian given by Eq. (2.1). The Monte Carlo algorithm chosen is a hybrid scheme, where each hybrid Monte Carlo step (MCS) consists of 10 updates each of which can be one of: one Metropolis sweep of the whole lattice, one single cluster

Wolff update,[29] or one overrelaxation update of the whole lattice.[8] The Metropolis algorithm updates the lattice sequentially in the standard way. According to the detailed balance condition we choose the acceptance probability $p(\beta\Delta E) = 1/[\exp(\beta\Delta E)+1]$ for a single spin flip, where ΔE is the change in configurational energy according to Eq. (2.1) and $\beta = 1/(k_B T)$.

The Wolff algorithm also works the standard way,[29] except that *only* the x and y components of the spins are used for the cluster growth. This means that a cluster update never changes the z component of any spin so that the Wolff algorithm is nonergodic in this case. Our cluster update is still a valid Monte Carlo step in the sense that it fulfills detailed balance, however, in order to provide a valid Monte Carlo algorithm it has to be used together with the Metropolis algorithm described above in a hybrid fashion. The use of Wolff updates allows us to take advantage of improved estimators[30] for magnetic quantities.

The overrelaxation part of the algorithm performs a microcanonical update of the configuration in the following way. The local configurational energy has the functional form of a scalar product of the spins, where according to Eq. (2.1) only the x and y components are involved. With respect to the sum of its nearest neighbor spins each spin has a transverse component in the xy plane which does not enter the scalar product. The overrelaxation algorithm simply scans the lattice sequentially, determines this transverse component for each lattice site and flips its sign. This does not change the local configurational energy ($\Delta E = 0$) and by virtue of the usual Metropolis acceptance function $f(\beta\Delta E) = \min[\exp(-\beta\Delta E),1]$ the update is always accepted. Along with this simple operation the sign of S_i^z is flipped with probability 1/2 at each lattice site which according to Eq. (2.1) also does not change the energy of the configuration. This overrelaxation algorithm is similar to the one used in Ref. 8 and it quite efficiently decorrelates subsequent configurations over a wider range of temperatures around the critical point than does the Wolff algorithm. Typically, we use three Metropolis (M), five single cluster Wolff (C), and two overrelaxation updates (O) in a hybrid Monte Carlo step in the critical region of our XY model. The inividual updates are mixed automatically in the program so that the update sequence ($MCCMOCMCCO$) is generated as one hybrid Monte Carlo step in this case. The random number generator we use is the shift register generator R1279 given by the recursion relation $X_n = X_{n-p} \oplus X_{n-q}$ for $(p,q) = (1279, 1063)$. Generators such as this are known to cause systematic errors in combination with the Wolff algorithm;[31] however, for lags (p,q) as large as the ones used here these errors will be far smaller than typical statistical errors. They are further reduced by the hybrid nature of our algorithm.[32]

The spin dynamics of the XY model is defined by the equations of motion

$$\frac{d}{dt}\mathbf{S}_k = \frac{\partial \mathcal{H}}{\partial \mathbf{S}_k} \times \mathbf{S}_k , \tag{2.2}$$

where $\mathcal{H}$ is the Hamiltonian defined by Eq. (2.1). One may interpret Eq. (2.2) as the direct classical analog of the Heisenberg equations of motion for spin operators, where $\hbar = 1$ so that energies and frequencies are measured in the same units. From the symmetry of Eq. (2.1) it is evident that the components M_x and M_y of the magnetization $\mathbf{M} = \Sigma_k \mathbf{S}_k$ are not conserved under the dynamics given by Eq. (2.2). Note that the two-component vector (M_x, M_y) is the *order parameter* of the XY model. The z or out-of-plane component M_z of the magnetization $\mathbf{M}$ is just the conserved quantity within the framework of model E dynamics we have already referred to in Sec. I.[3] Note that Eq. (2.1) is invariant with respect to the transformation $M_z \rightarrow -M_z$ which is a symmetry required by model E.

For the comparison of the critical spin dynamics with the critical dynamics according to model E it is important to realize, that the configurational *energy* is an *additional* constant of motion, because Eq. (2.2), in contrast to the coarse grained model E, does not contain relaxation. Whether energy conservation is a reasonable assumption for the dynamics of the XY model or any other classical spin model is a question of the time scales to be resolved. The most important time scale for our investigation is set by the propagating modes (spin waves) in the system and for these the configurational energy is indeed constant. Within the time scale of the spin waves thermal averages can therefore be replaced by averages over the initial configurations from which the time integration of Eq. (2.2) is started. For much longer times relaxation processes (equilibration with the heat bath) come into play which violate energy conservation and render our spin-dynamics approach invalid. In the vicinity of the critical point energy conservation becomes particularly important, because the dynamic universality class may change under the influence of an additional conservation law. If model E is augmented by energy conservation (model E', see Ref. 23) it turns out that the energy asymptotically decouples from the order parameter (M_x, M_y) and the conserved out-of-plane magnetization M_z and model E critical behavior is restored. However, energy conservation may introduce corrections to the asymptotic finite-size scaling behavior[23] which decay very slowly and may cause ambiguities in the scaling analysis of the spin-dynamics data. Note that these corrections are generated by the spin-dynamics method.

The equations of motion given by Eq. (2.2) are integrated numerically for each initial spin configuration by a recently developed decomposition method.[33] This method guarantees exact energy conservation and conservation of spin length $|\mathbf{S}_k| = 1$ and conserves M_z within its numerical truncation errors. For the present study a second order integrator is used with the time step $\delta t = 0.05/J$. This time step guarantees sufficient accuracy with respect to the conservation of M_z and is much faster than well-known predictor corrector methods.[4,33] For some accuracy and stability tests the time step has been increased to $\delta t = 0.1/J$ which still yields sufficient accuracy for the dynamic structure factor. Fourth order integrators are much more accurate as far as M_z conservation is concerned, but their internal complexity makes them much slower than a second order method for the same time step.[33] Moreover, statistical errors are not decrased significantly by fourth order methods and we therefore only report results obtained by the second order method. The equations of motion are integrated to a final time of $800/J$ and thermal averages are taken over 1000 initial configurations. All error bars of dynamic quantities correspond to one standard deviation. The simulations have been performed on various DEC alpha AXP, IBM

RS6000, and HP RISC8000 workstations both at the RWTH Aachen and the BUGH Wuppertal.

III. STATIC PROPERTIES OF THE *XY* MODEL

A. Thermodynamic properties

The basic ingredient for the spin-dynamics simulation is provided by the sequence of initial spin configurations, which has to be generated according to the canonical ensemble in order to provide well defined thermal averages. Therefore, the static behavior of the *XY* model and especially the location of T_c have to be determined first. For this purpose we employ the hybrid Monte Carlo scheme described above for lattice sizes L between $L=20$ and $L=80$. For each system size and temperature we perform 10 blocks of 10^3 hybrid steps for equilibration followed by 10^4 hybrid steps for measurements. Each measurement block yields an estimate for all static quantities of interest and from these we obtain our final estimates and estimates of their statistical error following standard procedures. The integrated autocorrelation time of our hybrid algorithm is determined by the autocorrelation function of the energy or, equivalently, the *modulus* $\sqrt{M_x^2+M_y^2}$ of the order parameter, which yield the slowest modes for the Wolff algorithm. The autocorrelation times are generally rather short, at T_c (see below) they range from about 5 hybrid MCS for $L=20$ to about 10 hybrid MCS for $L=80$. For comparison, the autocorrelation function for the order parameter itself yields an autocorrelation time of less than one hybrid MCS. The values for the equilibration and measurement periods given above thus translate to roughly 100 and 1000 autocorrelation times, respectively, which is sufficient for all practical purposes. In order to obtain the best statistics for magnetic quantities a measurement is made after every hybrid MCS.

The critical temperature T_c is determined by monitoring the temperature and size dependence of the Binder cumulant ratio. Specifically, we measure the cumulants

$$u_1=1-\frac{\langle M_x^4\rangle}{3\langle M_x^2\rangle^2} \quad \text{and} \quad u_2=1-\frac{\langle (M_x^2+M_y^2)^2\rangle}{3\langle M_x^2+M_y^2\rangle^2}. \tag{3.1}$$

It turns out that u_1 is more sensitive to changes in temperature and system size so that we only use u_1 for the final fine-tuning of the temperature T. For convenience the temperature is expressed as the dimensionless reduced coupling $K\equiv J/(k_BT)$, where $K_c\equiv J/(k_BT_c)$ denotes the critical point. From standard procedures[34] we obtain $K_c=0.64440\pm0.00005$. For comparison we mention that $K_c=0.45420\pm0.00002$ for the standard plane rotator *XY* model on a simple cubic lattice in $d=3$.[35] By ignoring corrections to scaling and averaging over the measurements for $L=40,\ 50,\ 60$, and 80 we find the estimates

$$u_1^*=0.3789\pm0.0015 \quad \text{and} \quad u_2^*=0.5859\pm0.0008 \tag{3.2}$$

for the values u_1^* and u_2^* of the cumulants defined by Eq. (3.1) at the critical point. Note that for $K=0.6444$ the value of u_1 remains within two standard deviations of u_1^* for all L. Our estimate for u_2^* is within two standard deviations of the corresponding estimate 0.5891 ± 0.0020 found in Ref. 35 which already gives some evidence that the planar Heisenberg variant of the *XY* model studied here is indeed a member of the static *XY* universality class.

The critical exponents are estimated from the critical finite-size scaling behavior of the average modulus $\langle\sqrt{M_x^2+M_y^2}\rangle$ of the order parameter, the average square $\langle M_x^2+M_y^2\rangle$ of the order parameter, and the temperature derivative of the latter. At $T=T_c$, i.e., $K=K_c$ one finds the leading scaling behavior

$$L^{-3}\langle\sqrt{M_x^2+M_y^2}\rangle\sim L^{-\beta/\nu}, \quad L^{-3}\langle M_x^2+M_y^2\rangle\sim L^{\gamma/\nu},$$
$$\frac{\partial}{\partial T}\ln\langle M_x^2+M_y^2\rangle\sim L^{1/\nu} \tag{3.3}$$

with the system size L, where β, γ, and ν are the critical exponents of the order parameter, the susceptibility, and the correlation length, respectively. During the data analysis it turns out that corrections to scaling can be ignored within the statistical error of the quantities in Eq. (3.3). From our estimate $K_c=0.6444$ and $L=20$, 24, 30, 36, 40, 50, 60, and 80 we find the following values for the critical exponents:

$$\beta/\nu=0.5179\pm0.0024, \quad \gamma/\nu=1.965\pm0.005,$$
$$1/\nu=1.494\pm0.013. \tag{3.4}$$

These values satisfy the scaling relation $2\beta/\nu+\gamma/\nu=d$. Furthermore, we directly obtain from Eq. (3.4) $\nu=0.6693\pm0.0058$, $\eta=0.035\pm0.005$, $\gamma=1.315\pm0.012$, and $\beta=0.3467\pm0.0034$ in very good agreement with previous Monte Carlo estimates[35] and renormalization group theory for the $O(N=2)$ Ginzburg-Landau model.[36] The critical exponent α of the specific heat can be obtained from, e.g., the hyperscaling relation, but the statistical error of ν is too large to exclude logarithmic behavior ($\alpha=0$). Apart from this deficiency our simulations confirm *XY*-like critical behavior for our version of the *XY* model [see Eq. (2.1)] quite accurately. In the following k_BT is measured in units of J chosen such that $k_BT_c=1$.

B. Static structure factor at criticality

We continue this section with a short discussion of the static spin-spin correlation function (structure factor) $G(\mathbf{q})$ at the critical temperature. The static structure factor is the spatial Fourier transform of the spin-spin correlation function

$$\mathcal{G}_{\alpha\beta}(\mathbf{R}_i-\mathbf{R}_j)\equiv\langle S_i^\alpha S_j^\beta\rangle-\langle S_i^\alpha\rangle\langle S_j^\beta\rangle, \tag{3.5}$$

where α,β refer to spin the components, $\mathbf{R}_i$ and $\mathbf{R}_j$ denote lattice vectors, and the thermal average is indicated by $\langle\cdots\rangle$. Note that $\mathcal{G}_{\alpha\beta}=\mathcal{G}_{\alpha\beta}(\mathbf{R}_i-\mathbf{R}_j)=\mathcal{G}_{\alpha\beta}(\mathbf{R}_j-\mathbf{R}_i)$ due to translational invariance and reflection symmetry of the system. The spatial Fourier transform is therefore given by a cosine transform which we use in the form

$$G_{\alpha\beta}(\mathbf{q})=\sum_i \mathcal{G}_{\alpha\beta}(\mathbf{R}_i)\cos\mathbf{q}\cdot\mathbf{R}_i\,. \tag{3.6}$$

With respect to the spontaneous magnetization of the *XY* model $G_{\alpha\beta}(\mathbf{q})$ has a transverse component $G_t(\mathbf{q})$ and a lon-

gitudinal component $G_l(\mathbf{q})$. In our Monte Carlo simulation we measure G_t and G_l by *rotating* the coordinate system of the spins around the z axis such that the random but finite magnetization vector (M_x, M_y) is aligned with the y direction. The x and y components of the spins in the rotated frame then correspond to the transverse and the longitudinal spin components, respectively, and their correlation functions yield $G_t \equiv G_{xx}$ and $G_l \equiv G_{yy}$. It should also be mentioned that the out-of-plane component $G_{zz}(\mathbf{q})$ of the static structure factor is independent of $\mathbf{q}$ and does not show any critical behavior. According to Eq. (3.6) the normalization of $G_{\alpha\beta}(\mathbf{q})$ is such that $G_{\alpha\beta}(\mathbf{q}=\mathbf{0}) = k_B T \chi_{\alpha\beta}$, where $\chi_{\alpha\beta}$ is the static susceptibility. Note that $G_t(\mathbf{q}=\mathbf{0}) = 0$ by definition and that $G_l(\mathbf{q}=\mathbf{0}) = k_B T \chi'$, where χ' is the magnetic susceptibility with respect to the *modulus* of the magnetization. We furthermore limit the discussion to the (100) direction, because other lattice directions do not provide new information on a simple cubic lattice. The components of $\mathbf{q}$ are always measured in units of the inverse lattice contant.

At T_c the longitudinal component $G_l(\mathbf{q})$ of the static structure factor can be described by the model function

$$G_l[\mathbf{q}=(q,0,0)] = L^{2-\eta} g_l(qL) h(q), \tag{3.7}$$

where $2-\eta = \gamma/\nu$ is taken from Eq. (3.4), $h(q) = [(q/2)/\sin(q/2)]^2$ captures lattice effects,[37] and the finite-size scaling function $g_l(x)$ is chosen as a simple generalization of a Lorentzian

$$g_l(x) = a^{-(2-\eta)} [1 + (x/b)^2]^{-(2-\eta)/2}. \tag{3.8}$$

The parameters a and b are determined from a fit to the data, where a and b are independent of L. We have chosen $a = 3.70$ and $b = 4.35$ as obtained from a fit to the data for $L = 60$. For $L = 40$ and $L = 80$ a and b are found within less than 1% of these values, for $L = 20$ they are about 3% smaller. Despite its simplicity the model function given by Eq. (3.7) captures the shape of the Monte Carlo estimate for the longitudinal component of the structure factor remarkably well. The finite-size scaling analysis of our data for $G_l(\mathbf{q})$ for small q, is shown in Fig. 1. Deviations from finite-size scaling set in at $qL = 4\pi$ for $L = 20$, the data for $L = 40$, 60, and 80 collapse within the error bars up to $qL = 6\pi$. Within the symbol sizes data collapse is obtained up to $qL = 10\pi$, where lattice effects set in. For comparison the model scaling function $g_l(qL)$ [$a = 3.70$ and $b = 4.35$, see Eq. (3.8)] is shown by the dashed line in Fig. 1. The true scaling form of $G_l(\mathbf{q})$ for small q is captured rather well by $g_l(x)$. However, the choice of the model function is, of course, not unique.

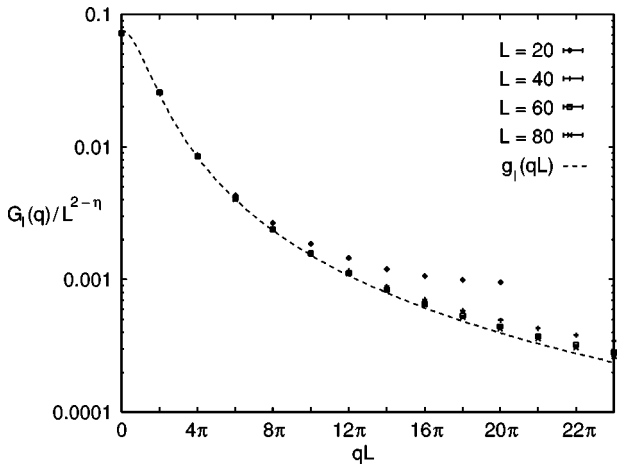

FIG. 1. Scaling plot for $G_l(\mathbf{q})/L^{2-\eta}$ at $T = T_c$ for $L = 20$ ($\diamond$), 40 ($+$), 60 ($\square$), and 80 ($\times$) as a function of qL with $\eta = 0.035$. Statistical errors of the data are much smaller than the symbol sizes. The dashed line displays the scaling function $g_l(qL)$ as given by Eq. (3.8) for $a = 3.70$ and $b = 4.35$. Note that $qL = 20\pi$ corresponds to the Brillouin zone boundary for $L = 20$.

IV. THE DYNAMIC STRUCTURE FACTOR

The dynamic structure factor $S(\mathbf{q},\omega)$ is the space-time Fourier transform of the position and time displaced spin-spin correlation function $\mathcal{S}_{\alpha\beta}(\mathbf{R}_i - \mathbf{R}_j, |t-t'|)$ which we define by [see Eq. (3.5)]

$$\mathcal{S}_{\alpha\beta}(\mathbf{R}_i - \mathbf{R}_j, |t-t'|) \equiv \langle S_i^\alpha(t) S_j^\beta(t') \rangle - \langle S_i^\alpha(t) \rangle \langle S_j^\beta(t') \rangle. \tag{4.1}$$

The indices α,β refer to spin components, $\mathbf{R}_i$ and $\mathbf{R}_j$ are lattice vectors, and t and t' are moments in time to which the initial spin configuration has evolved according to the equations of motion [see Eq. (2.2)]. The average $\langle \cdots \rangle$ is taken over the set of initial configurations as described in Sec. II. Note that $\mathcal{S}_{\alpha\beta}$ is also symmetric with respect to $\mathbf{R}_i$ and $\mathbf{R}_j$ [see Eq. (3.5)]. As the second argument only the time displacement enters, because the equations of motion are invariant under the transformation $\mathbf{S}_i \to -\mathbf{S}_i$, $t \to -t$ [see Eqs. (2.1) and (2.2)]. The space-time Fourier transform is therefore also given by the cosine transform [see Eq. (3.6)]

$$S_{\alpha\beta}(\mathbf{q},\omega) = 2/\pi \int_0^\infty \sum_i \mathcal{S}_{\alpha\beta}(\mathbf{R}_i, |t|) \cos \mathbf{q}\cdot\mathbf{R}_i \cos \omega t dt. \tag{4.2}$$

Note that the normalization in Eq. (4.2) is such that $\int_0^\infty S_{\alpha\beta}(\mathbf{q},\omega) d\omega = G_{\alpha\beta}(\mathbf{q})$, where $G_{\alpha\beta}(\mathbf{q})$ is the static structure factor defined by Eq. (3.6).

The out-of-plane component $S_{zz}(\mathbf{q},\omega)$ of the dynamic structure factor is associated with the conserved out-of-plane magnetization M_z, i.e., $\Sigma_i \mathcal{S}_{zz}(\mathbf{R}_i, |t|)$ [see also Eq. (4.2)] is a constant in time. The in-plane magnetization (order parameter) (M_x, M_y) is not conserved under the spin dynamics. Although the time scale set by the motion of M_x and M_y is considerably larger than typical time scales set by spin waves, all initial differences between longitudinal and transverse components of the spin correlations completely disappear during the integration of the equations of motion. We therefore only discuss the average of the xx and the yy component of $S(\mathbf{q},\omega)$ and refer to it as the ''in-plane component'' $S_{xx}(\mathbf{q},\omega)$.

We now turn to the discussion of $S(\mathbf{q},\omega)$ above, below, and at the critical point. The correlation functions are measured up to a time displacement of $400/J$ away from criticality, where only smaller systems are considered. At the critical temperature we measure correlations up to $600/J$ for systems with up to $L = 60$ lattice sites in each direction.

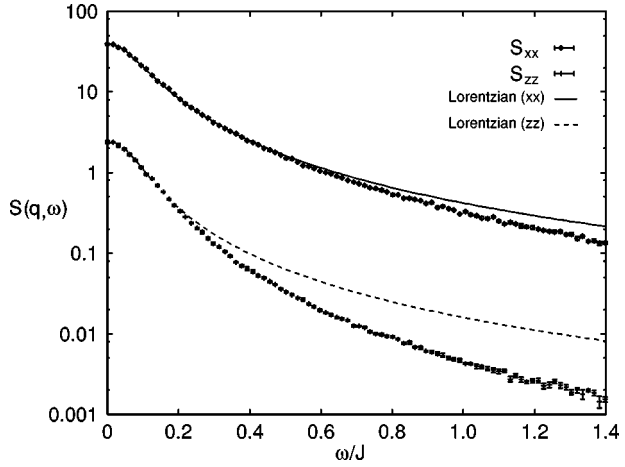

FIG. 2. In-plane component S_{xx} ($\diamond$) and out-of-plane component S_{zz} ($+$) of the dynamic structure factor in the (100) direction for $T=1.1T_c$, $L=30$, and $q=\pi/15$ as functions of the dimensionless frequency ω/J. For small enough ω the line shapes are well approximated by Lorentzians given by Eq. (4.3) (solid line) and Eq. (4.4) (dashed line), respectively. The ranges over which the Lorentzian approximation is valid differ significantly for S_{xx} and S_{zz}.

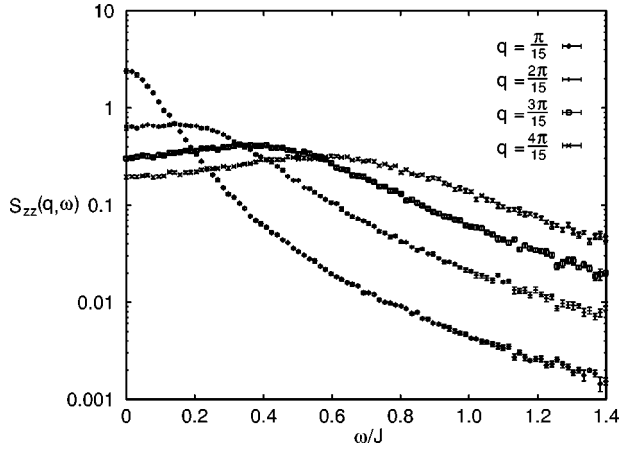

FIG. 3. Out-of-plane component S_{zz} of the dynamic structure factor in the (100) direction for $T=1.1T_c$, $L=30$, and $q=\pi/15$ ($\diamond$), $q=2\pi/15$ ($+$), $q=3\pi/15$ ($\square$), $q=4\pi/15$ ($\times$) as a function of the dimensionless frequency ω/J.

A. The structure factor above T_c

In order to avoid effects of criticality we choose the temperature $T=1.1T_c$ in the following. Due to the absence of critical finite-size scaling at this temperature we limit the spin-dynamics simulations to smaller systems with $L=20$, 24, and 30. For better momentum resolution we only present results obtained for $L=30$, smaller L yield identical results with a lower resolution in $\mathbf{q}$. We also limit the presentation to $S(\mathbf{q},\omega)$ in the (100) direction, other lattice directions provide essentially the same information. In Fig. 2 we show $S_{xx}[\mathbf{q}=(q,0,0),\omega]$ and $S_{zz}[\mathbf{q}=(q,0,0),\omega]$ for $q=\pi/15$ as functions of the dimensionless frequency ω/J. Both components apparently display a central peak without any additional features. For the values of T and q used in Fig. 2 one expects a central peak of Lorentzian shape.[22] As displayed by the solid line in Fig. 2 a simple Lorentzian of the form

$$L_{xx}(q,\omega)=\frac{A^0_{xx}(q)}{1+[\omega/\Gamma^0_{xx}(q)]^2} \tag{4.3}$$

characterized by an amplitude $A^0_{xx}(q)$ and a width $\Gamma^0_{xx}(q)$ captures the shape of S_{xx} very well up to $\omega/J\simeq 0.4$, where the intensity has already dropped by an order of magnitude. For larger ω S_{xx} decays faster than a Lorentzian. If one tries to fit the line shape of S_{zz} also with a Lorentzian for small ω, it turns out that a better fit is obtained from a superposition of symmetrically placed Lorentzians. We use

$$L_{zz}(q,\omega)=\frac{A_{zz}(q)}{1+\{[\omega-\omega(q)]/\Gamma_{zz}(q)\}^2} + \frac{A_{zz}(q)}{1+\{[\omega+\omega(q)]/\Gamma_{zz}(q)\}^2}, \tag{4.4}$$

where $\omega(q)$ denotes the spin wave frequency which is used as an additional fit parameter. The dashed line in Fig. 2 displays the Lorentzian fit for S_{zz} according to Eq. (4.4), where $\omega(\pi/15)\simeq 0.030$ is indeed finite within its statistical error of roughly 10^{-3}. However, Eq. (4.4) only captures the shape of S_{zz} up to $\omega/J\simeq 0.15$. If Eq. (4.3) [$\omega(\pi/15)=0$] is used instead, this frequency range becomes even smaller. This discrepancy in frequency range between the in-plane and the out-of-plane components of $S(\mathbf{q},\omega)$ may be due to the difference in time scales between in-plane and out-of-plane modes as predicted by mode coupling theory.[22]

Spin-wave signatures are still visible in S_{zz} at $T=1.1T_c$ as shown in Fig. 3, where S_{zz} is plotted for the first four momenta $q=n\pi/15$, $n=1,2,3,4$. For $n\geq 2$ a very broad maximum becomes visible which moves to the right as q increases. The appearance of spin-wave signatures in S_{zz} above T_c is expected from renormalization group theory for model E dynamics.[25] For the q values used in Fig. 3 the shape of S_{zz} is captured quite well by the Lorentzian defined by Eq. (4.4). Due to the small enhancement of the line intensity over the signal level at $\omega=0$ the peak position $\omega(q)$ and linewidth $\Gamma_{zz}(q)$ are not very well defined. We therefore refrain from a more detailed analysis at this point. The frequency dependence of the in-plane component S_{xx} is dominated by a central peak as in Fig. 2 for all q. Only for large q near the Brillouin zone boundary a shoulder appears in S_{xx} near the position of the spin-wave peak in S_{zz}. We illustrate this in Fig. 4, where S_{xx} and S_{zz} are shown for $q=\pi$. Note that S_{zz}, which is much smaller than S_{xx} for small q (see Fig. 2), becomes comparable to S_{xx} in magnitude for large q. In a qualitative sense we have recovered the same behavior as observed by spin-dynamics simulations of the XY model in $d=2$ above the Kosterlitz-Thouless transition.[20]

B. The structure factor below T_c

As before we want to avoid critical finite-size effects also below T_c and we therefore choose $T=0.9T_c$ in the following. Again relatively small systems are sufficient for this investigation. Our main results have been obtained for $L=30$, smaller systems yield the same results at a lower q resolution. The dynamics of the XY model below T_c is dominated by spin waves which are visible in $S(\mathbf{q},\omega)$ as pronounced peaks at the spin wave frequency $\omega(q)$ as shown in

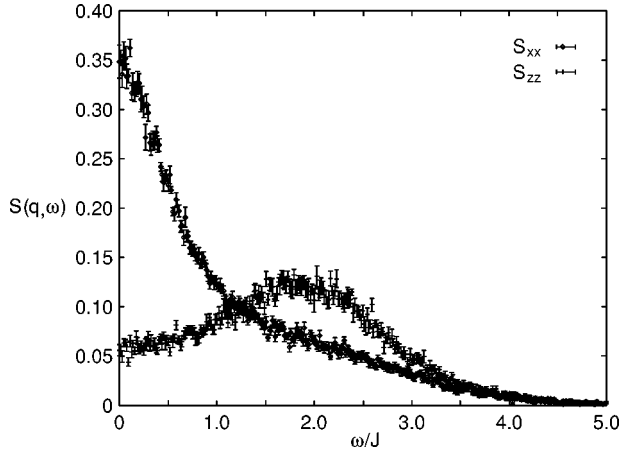

FIG. 4. In-plane component S_{xx} ($\diamond$) and out-of-plane component S_{zz} ($+$) of the dynamic structure factor in the (100) direction for $T=1.1T_c$, $L=30$, and $q=\pi$ as functions of the dimensionless frequency ω/J. A shoulder appears at the position of the spin wave peak in S_{zz}.

Fig. 5 for $q=\pi/15$ in the (100) direction. The peak intensity of S_{xx} is more than one order of magnitude larger than the corresponding peak intensity of S_{zz}. S_{xx} also displays a pronounced central peak, where the intensity exceeds the intensity of S_{zz} by over three orders of magnitude. In a qualitative sense this is again the same behavior as observed in $d=2$,[20] where the central peak in S_{xx} was not expected by analytical theory.[16] We also find some ''fine structure'' at low intensities in S_{xx} for which no theoretical predictions exist. In Fig. 5 we have marked these additional resonances by arrows. As demontrated already in $d=2$ (Ref. 20) these signals can be interpreted as two-spin wave peaks in the following way. In order to produce a contribution to S_{xx} at $q=\pi/15$ in the (100) direction one can combine *two* spin waves at $q=\pi/15$, one in the (010) direction, which is eqivalent to the (100) direction on a simple cubic lattice, and one in the (110) direction (not shown), where the latter has a higher

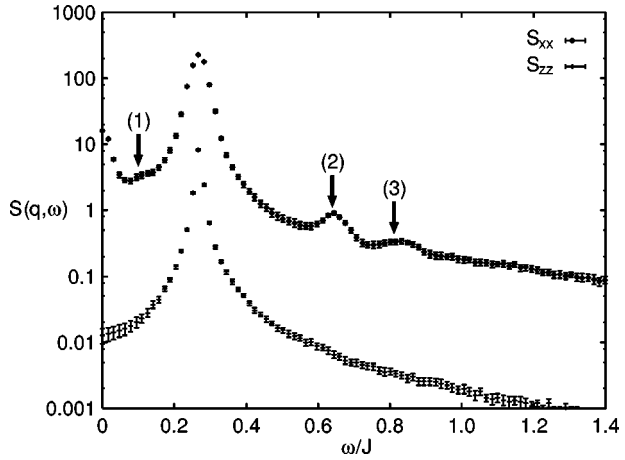

FIG. 5. In-plane component S_{xx} ($\diamond$) and out-of-plane component S_{zz} ($+$) of the dynamic structure factor in the (100) direction for $T=0.9T_c$, $L=30$, and $q=\pi/15$ as functions of the dimensionless frequency ω/J. Apart from the dominant spin wave peak additional resonances appear in S_{xx} (arrows) at low intensities (see main text).

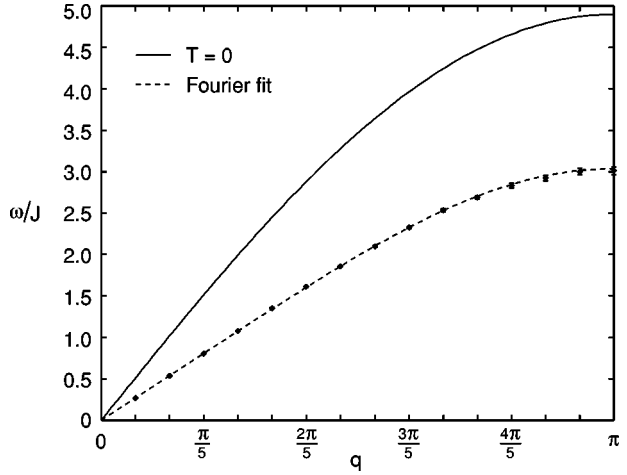

FIG. 6. Dispersion relation $\omega(q)$ ($\diamond$) in the (100) direction for $T=0.9T_c$ and $L=30$. The solid line is the $T=0$ dispersion relation obtained from linear spin wave theory [see Eq. (4.6)]. The dashed line is a fit to the first two terms of the Fourier series given by Eq. (4.7).

energy (frequency). The *difference* between the corresponding frequencies is marked as (1) in Fig. 5, their *sum* is marked as (2). A second way to get a contribution to S_{xx} at $q=\pi/15$ in the (100) direction is to combine two spin waves in the (100) direction, one at $q=\pi/15$ the other at $q=2\pi/15$, where again the latter has a higher energy. The *sum* of the corresponding frequencies is marked as (3) in Fig. 5 their *difference* almost coincides with the position of the spin wave peak and can therefore not be resolved.

In order to monitor the q dependence of the spin wave frequency $\omega(q)$ and the line widths $\Gamma_{xx}(q)$ and $\Gamma_{zz}(q)$ of the spin-wave peaks, we again employ fits to simple Lorentzians. For the in-plane component we generalize Eq. (4.3) to include the spin-wave peaks

$$L_{xx}(q,\omega)=\frac{A^0_{xx}(q)}{1+[\omega/\Gamma^0_{xx}(q)]^2}+\frac{A_{xx}(q)}{1+\{[\omega-\omega(q)]/\Gamma_{xx}(q)\}^2}+\frac{A_{xx}(q)}{1+\{[\omega+\omega(q)]/\Gamma_{xx}(q)\}^2}. \tag{4.5}$$

For the out-of-plane component we use Eq. (4.4) which captures the shape of S_{zz} for sufficiently small frequencies in a satisfactory way. The dispersion relation $\omega(q)$ can be obtained from Eq. (4.5) or Eq. (4.4), where the latter yields slightly smaller error bars, because S_{zz} displays a sharper spin-wave maximum. The estimates for $\omega(q)$, $\Gamma_{xx}(q)$, and $\Gamma_{zz}(q)$ depend on the frequency range over which Eqs. (4.5) and (4.4) are fitted to S_{xx} and S_{zz}, respectively. We have chosen a frequency window around the spin-wave peak, where for S_{xx} the central peak has been subtracted first. The error in the dispersion relation and the line widths is estimated by varying the size of the frequency window from about 1.2 times the half width to about twice the half width of the peak. The dispersion relation $\omega(q)$ obtained from this procedure for the (100) direction is shown in Fig. 6, the correponding zero temperature dispersion relation is shown by the solid line. According to linear spin-wave theory one obtains

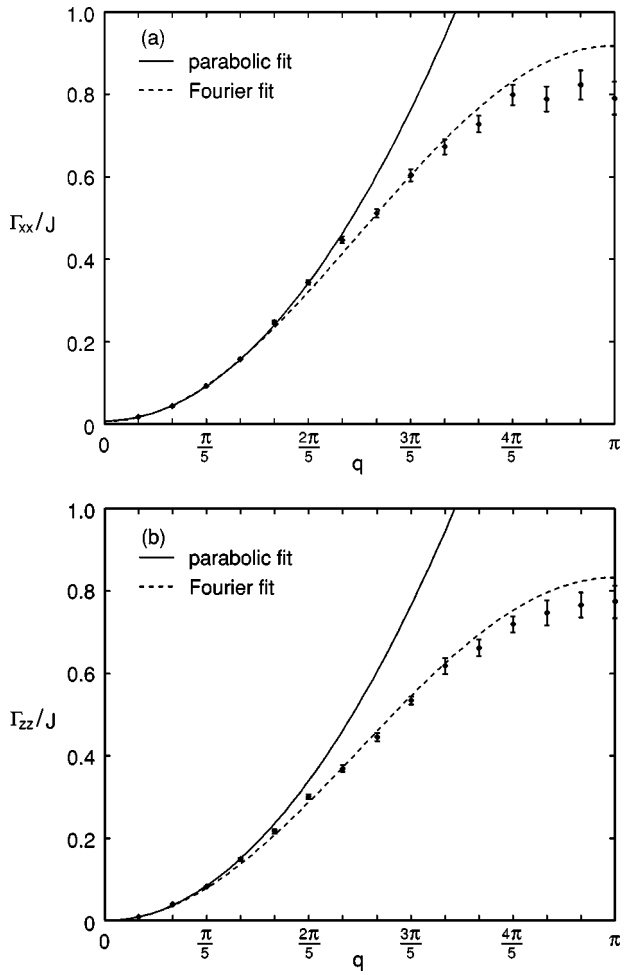

FIG. 7. Linewidths (a) $\Gamma_{xx}(q)$ and (b) $\Gamma_{zz}(q)$ of the spin-wave peak in S_{xx} for the (100) direction, $T=0.9T_c$, and $L=30$. The solid lines are parabolic fits to the first four data points (see Fig. 8). The dashed lines are fits with the first two terms of the Fourier series given by Eq. (4.8).

$$\omega(q)/J=2\sqrt{2d}\,\sin(q/2), \tag{4.6}$$

for $T=0$ where $d=3$ in our case. As expected, the spin wave frequencies are ''renormalized'' to fall below the $T=0$ dispersion curve. The functional form of $\omega(q)$ can be captured by a Fourier series. A convenient choice is

$$\omega(q)/J=a_1\sin(q/2)+a_2\sin(3q/2)+a_3\sin(5q/2)+\cdots, \tag{4.7}$$

where the Fourier coefficients $a_1,a_2,a_3,\ldots$, are rapidly decreasing. If Eq. (4.7) is truncated after the second term one obtains $a_1=2.919$ and $a_2=-0.116$ from a least square fit which connects all data points within their error bars as shown by the dashed line in Fig. 6.

The linewidth $\Gamma_{xx}(q)$ of the spin wave peak in the in-plane component of the structure factor is shown in Fig. 7(a). As before the data can be analyzed by a Fourier series with rapidly decreasing coefficients. A convenient choice here is

$$\Gamma_{\alpha\alpha}(q)/J=b_0+b_1\cos q+b_2\cos 2q+\cdots, \tag{4.8}$$

where α refers to x (in-plane) and z (out-of-plane). A fit to Γ_{xx} with only two coefficients yields $b_0=0.4622$ and $b_1=-0.4559$ which is shown by the dashed line in Fig. 7(a). The statistical error of b_0 and b_1 is about 5×10^{-4}. The data for small q are represented quite well, whereas near the Brillouin zone boundary significant deviations occur. These can be reduced very quickly by including higher Fourier modes in the fit (not shown), where the higher Fourier coefficients decrease rapidly in magnitude. Here, we are primarily interested in the q dependence of the linewidth near the center of the Brillouin zone (see below). A corresponding analysis has been performed for the linewidth $\Gamma_{zz}(q)$ of the spin wave peak in the out-of-plane component of the structure factor. The result is shown in Fig. 7(b), where the Fourier coefficients in the fit (dashed line) are given by $b_0=0.4160(5)$ and $b_1=-0.4165(5)$. Again the small q behavior is captured very well by the fit, but near the Brillouin zone boundary deviations occur which can also be reduced very quickly by including higher Fourier modes.

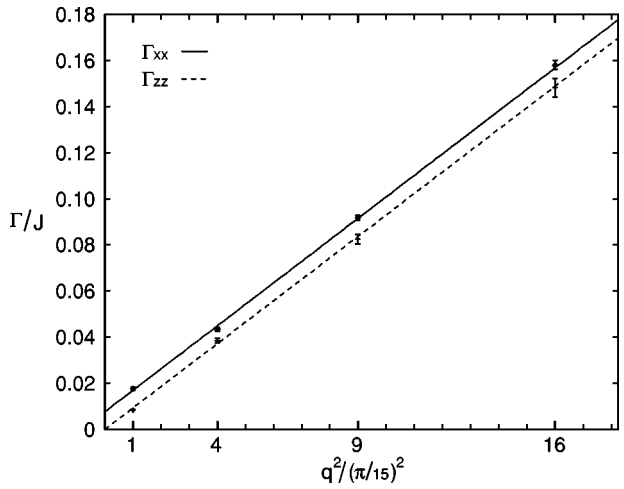

FIG. 8. Extrapolation of the linewidths $\Gamma_{xx}(q)$ (solid line) and $\Gamma_{zz}(q)$ (dashed line) to $q=0$. The linewidths vary as q^2 for small q as predicted by mode coupling theory (see main text).

The limit $q\to0$ is of particular interest for the linewidths, because it reflects the influence of conservation laws on the dynamics. The linewidth $\Gamma_{xx}(q=0)$ can be interpreted as the relaxation rate of the (nonconserved) order parameter and therefore $\Gamma_{xx}(q=0)$ should be positive. The linewidth $\Gamma_{zz}(q=0)$ is the relaxation rate of the out-of-plane magnetization M_z which is *conserved*, i.e., $\Gamma_{zz}(q=0)$ should *vanish*. From the Fourier fits shown in Fig. 7 one finds $\Gamma_{xx}(0)\simeq0.0063$ and $\Gamma_{zz}(0)\simeq-0.0005$ with statistical errors of about 7×10^{-4} in both cases. The extrapolation of $\Gamma_{xx}(q)$ and $\Gamma_{zz}(q)$ to $q=0$ is shown in Fig. 8. The q dependence of the linewidths for small q is quadratic as anticipated by the Fourier fits shown in Fig. 7. From a fit to a straight line we find $\Gamma_{xx}(0)=0.0076\pm0.0006>0$ (solid line), whereas $\Gamma_{zz}(0)=0$ (dashed line) within its statistical error in agreement with the conservation laws. Finally, we note that the q^2 dependence of the linewidth Γ_{zz} is in agreement with the prediction of mode coupling theory.[22]

C. The structure factor at T_c

The exploration of critical dynamics and dynamic scaling naturally requires most of the numerical effort. In order to reach the scaling regime large systems are required and we

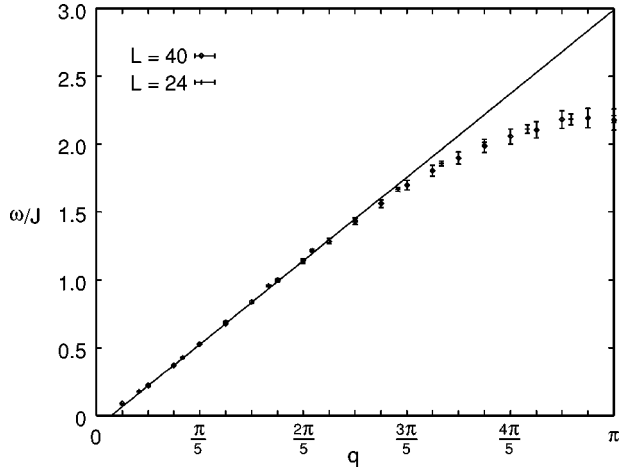

FIG. 9. Dispersion relation $\omega_{zz}(q)$ in the (100) direction for $T=T_c$ and $L=24$ (+) and 40 ($\diamond$). The solid line displays a linear extrapolation of the data for $q<\pi/2$ to $q=0$. Deviations from linearity become visible only for $q\leqslant\pi/20$ where critical effects set in.

have therefore performed simulations for $L=20$, 24, 30, 40, and 60. Our prime objective here is the test of dynamic finite-size scaling which we assume to be valid in the form[8,20]

$$S_{\alpha\alpha}(\mathbf{q},\omega)/G_{\alpha\alpha}(\mathbf{q})=L^{z_\alpha}\Sigma_{\alpha\alpha}(qL,\omega L^{z_\alpha}) \tag{4.9}$$

at the critical point, where $G_{\alpha\alpha}$ is the static structure factor discussed in Sec. III and z_α denotes the dynamic critical exponent. Note, that the $\mathbf{q}$ dependence is reduced to a dependence only on $q=|\mathbf{q}|$, i.e., isotropic scaling in space has been assumed. The index α again refers to the spin component x (in-plane) or z (out-of-plane), where $z_x\equiv z_\phi$ and $z_z\equiv z_m$, respectively. In order to estimate z_α we scale our data according to Eq. (4.9) and test the result for data collapse in the limit of small frequencies. The static structure factor needed for normalization in Eq. (4.9) is given by the equal-time correlations which we also extract from the spin-dynamics data for consistency.

In order to provide numerical estimates of the dynamic exponents z_m and z_ϕ first we analyze the dispersion relations $\omega_{zz}(q)$ and $\omega_{xx}(q)$ at the critical point as obtained from a Lorentz fit to the spin-wave peak of $S_{zz}(q,\omega)$ [see Eq. (4.4)] and a Lorentz fit to $S_{xx}(q,\omega)$ according to Eq. (4.3). The line shape of S_{xx} is dominated by a strong central peak (see below) so that we restrict the analysis of the full dispersion relation to $\omega_{zz}(q)$. The result in the (100) direction is shown in Fig. 9 for $L=24$ and $L=40$. The data apparently collapse onto a single curve and show a linear behavior for $q<\pi/2$ down to $q\simeq\pi/20$, where $\omega(q)$ becomes nonlinear. From finite-size scaling one expects the scaling form

$$\omega_{\alpha\alpha}=q^{z_\alpha}\Omega_\alpha(qL) \tag{4.10}$$

at T_c for sufficiently small q. For $qL=2\pi$ and $L=20$, 24, 30, 40, and 60 we obtain an approximation of the small q behavior of ω_{zz} which is shown in Fig. 10(a). According to Eq. (4.10) ω_{zz} should vary as q^{z_m} for fixed qL. A least square fit to the data shown in Fig. 10(a) yields the dynamic exponent

$$z_m=1.38\pm0.05 \tag{4.11}$$

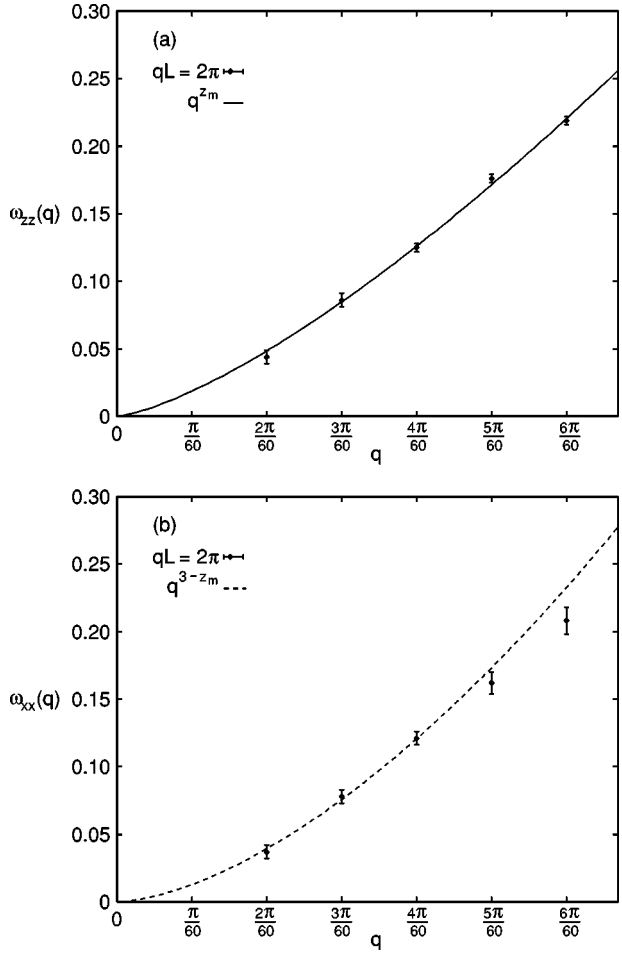

FIG. 10. Small q behavior of the dispersion relations (a) $\omega_{zz}(q)$ and (b) $\omega_{xx}(q)$ in the (100) direction for $T=T_c$. The solid line is a power law fit to the data which yields $z_m=1.38\pm0.05$. The dashed line is a power law with the exponent $z_\phi=3-z_m=1.62\pm0.05$. The data for the smallest systems $L=20$ and $L=24$ deviate systematically from the power law.

which differs substantially from the mode-coupling prediction $z_m=z_\phi=1.5$.[22] From the scaling relation $z_\phi=3-z_m$ (Refs. 24,25,28) we obtain $z_\phi=1.62\pm0.05$ which can be tested against the small q behavior of $\omega_{xx}(q)$. The result is shown in Fig. 10(b). For the larger systems $L=30$, 40, and 60 the data agree with the power law, but for smaller lattice sizes $L=20$ and $L=24$ systematic deviations occur. If we exclude these smaller systems from the power-law fit shown in Fig. 10(a) we find $z_m=1.43\pm0.14$ which is at the upper error boundary of the previous estimate given by Eq. (4.11). An alternative estimate of the dynamic exponents is provided by the *median frequency* $\omega^M_{\alpha\alpha}$ which is defined by the relation

$$\int_0^{\omega^M_{\alpha\alpha}} S_{\alpha\alpha}(\mathbf{q},\omega)\,d\omega=\frac{1}{2}G_{\alpha\alpha}(\mathbf{q}). \tag{4.12}$$

Note that we have normalized the dynamic structure factor such that its integral over all frequencies yields the static structure factor. We evaluate Eq. (4.12) with the trapezoidal rule. Systematic errors induced by this simple numerical integration method are smaller than statistical uncertainties coming from the statistical errors of $S_{xx}(q,\omega)$ and $S_{zz}(q,\omega)$.

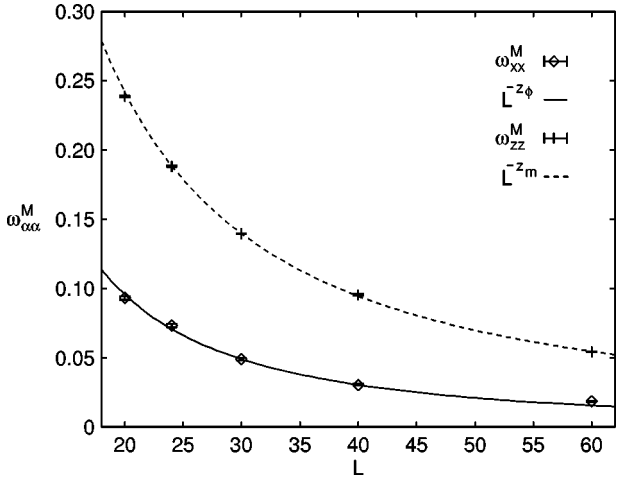

FIG. 11. Median frequencies ω^M_{xx} ($\diamond$, solid line) and ω^M_{zz} ($+$, dashed line) for $qL=2\pi$. The solid and dashed lines display fits to power laws [see Eq. (4.13)].

If the integration is performed with Simpsons rule the same results are obtained within statistical errors. According to Eq. (4.9) we expect the scaling behavior

$$\omega^M_{\alpha\alpha}=L^{-z_\alpha}M_{\alpha\alpha}(qL) \tag{4.13}$$

of the median frequency at the critical point. Due to the presence of a strong central peak in $S_{xx}(q,\omega)$ the median frequency ω^M_{xx} for $L=60$ turns out to be of the same size as the frequency resolution of our data. We therefore limit the analysis of ω^m_{xx} to the system sizes $L=20$, 24, 30, and 40. The other median frequency ω^m_{zz} can be determined accurately for all system sizes. The result for $qL=2\pi$ is displayed in Fig. 11. From a least square fit of ω^M_{xx} to a power law for $L=20$, 24, 30, and 40 we obtain $z_\phi=1.61\pm0.03$. If only the data for $L=30$ and 40 are used we obtain $z_\phi=1.65\pm0.10$. Both estimates are consistent with Eq. (4.11) and the scaling relation $z_\phi+z_m=3$. The latter estimate is displayed by the solid line in Fig. 11. The corresponding fit of ω^M_{zz} for $L\geqslant30$ yields $z_m=1.35\pm0.01$ which is also within the error bar of our previous estimate [see Eq. (4.11), dashed line in Fig. 11]. The spread in the values for the dynamic exponents obtained from the dispersion relations for small q and the median frequencies is considerable. In order to reconcile all estimates with Eq. (4.11) almost the full width of the error interval (one standard deviation) is needed. However, Eq. (4.11) represents a reasonable mean value of all estimates discussed so far and we therefore adopt it as our final estimate for z_m and use $z_\phi+z_m=3$ to determine z_ϕ.

As a final test of Eq. (4.11) we use Eq. (4.9) in order to obtain a scaling plot of the dynamic structure factor. For $qL=2\pi$, $L=30$, 40, and 60 and $z_m=1.38$ the resulting scaling plot for $S_{zz}(q,\omega)$ is shown in Fig. 12. The corresponding plot for $S_{xx}(q,\omega)$ with $z_\phi=3-z_m=1.62$ is displayed in Fig. 13. Data collapse can only be expected for sufficiently small ω. Scaling works quite well for all frequencies up to the spin wave peak, where the intensity decreases slightly with increasing L, but the error bars are still overlapping. The quality of the data collapse in not so evident from $S_{xx}(q,\omega)$ (see Fig. 13). At $\omega=0$ the scaled intensity for $L=60$ deviates from the ones for $L=30$ and 40 by about one standard deviation. This could be an effect of the finite statistical sample. The line shape of the central peak in S_{xx} still fits rather well to a Lorentzian. Only in the vicinity of $\omega=0$ are the data also compatible with the Gaussian line shape expected from mode coupling theory.[22]

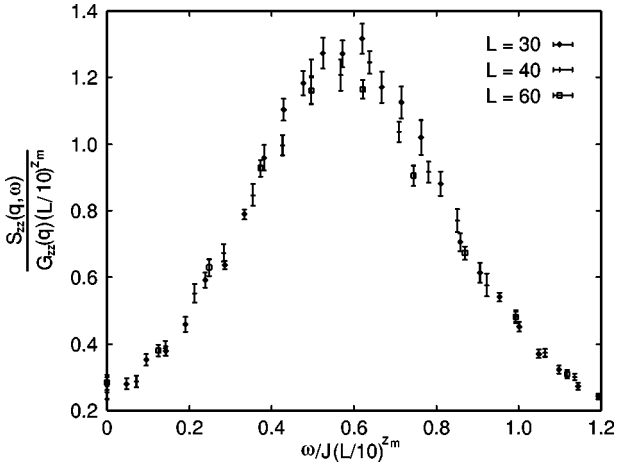

FIG. 12. Scaling plot of $S_{zz}(q,\omega)/[(L/10)^{z_m}G_{zz}(q)]$ versus $\omega/J(L/10)^{z_m}$ for $qL=2\pi$ and system sizes $L=30$, 40, and 60.

The above scaling analysis provides quite strong evidence for a violation of dynamic scaling in the sense that two different dynamic exponents are required in order to obtain scaling in the dispersion relations, the median frequencies, and the two components of the dynamic structure factor. However, we cannot prove from our data whether the estimate $\omega_w=z_\phi-z_m=0.24$, which indicates the violation of dynamic scaling, corresponds to the transient exponent ω_w (Refs. 25,28) or if the measured difference consitutes an *effective* exponent for system sizes which are too small to ignore additional corrections. As pointed out in Sec. I the presence of energy conservation in our spin-dynamics simulation gives rise to such corrections governed by the exponent α/ν.[23] On the basis of our data we cannot exclude the possibility, that these corrections yield the dominant contribution to the measured effective exponent ω_w. For a clarification of this point more information is needed from analytical theories of dynamic finite-size scaling[38] and from simulations.[39]

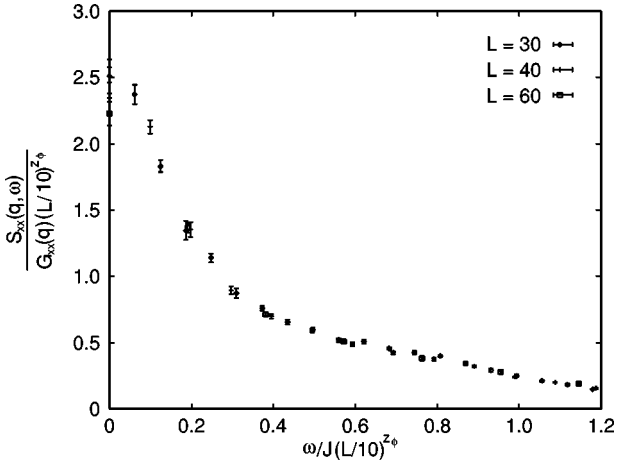

FIG. 13. Scaling plot of $S_{xx}(q,\omega)/[(L/10)^{z_\phi}G_{xx}(q)]$ versus $\omega/J(L/10)^{z_\phi}$ for $qL=2\pi$ and system sizes $L=30$, 40, and 60.

V. SPIN TRANSPORT AND THERMAL CONDUCTIVITY

We have already mentioned in the Introduction that the transport properties of the XY model near the critical point provide lattice analogues of the corresponding transport coefficients of ^{4}He near the λ transition. The conserved out-of-plane component M_z of the magnetization is the lattice analog of the entropy density in ^{4}He and its associated transport coefficient therefore corresponds to the thermal conductivity of ^{4}He which is of experimental interest. In principle the thermal conductivity can be extracted from an extrapolation of the characteristic frequency ω_0 of S_{zz} given by $\omega_0^{-1} = \frac{1}{2} S_{zz}(q,0)$ (Refs. 25,40) to $q=0$. However, in order to obtain a reliable extrapolation at the critical point a very high momentum resolution for $q \to 0$ is required and this can only be realized with very large systems (see Fig. 9 and Ref. 40). We therefore resort to an alternative approach already considered in Ref. 40, we express the thermal conductivity by a current-current correlation function for a suitably chosen current density $\mathbf{j}_k = (j_{1,k}, j_{2,k}, j_{3,k})$ at lattice site k.[41]

In order to identify the current density $\mathbf{j}_k$ we reexamine the z component of the equation of motion [see Eq. (2.2)] which reads

$$\frac{d}{dt} S_k^z = -J \sum_{l \in NN(k)} (S_l^x S_k^y - S_l^y S_k^x), \tag{5.1}$$

where the sum is over all nearest neighbors of lattice site k. We define the ith component $j_{i,k}$ $(i=1,2,3)$ of the current density $\mathbf{j}_k$ associated with the lattice point k by[40]

$$j_{i,k} \equiv J(S_k^y S_{k+e_i}^x - S_k^x S_{k+e_i}^y), \tag{5.2}$$

where the notation $k+e_i$ denotes the nearest neighbor of the lattice site k in the ith lattice direction. For the case of the simple cubic lattice studied here e_1, e_2, and e_3 can be visualized as the unit vectors of a Cartesian coordinate system aligned with the lattice. The lattice divergence of the current density according to Eq. (5.2) at lattice site k is then given by

$$\nabla \cdot \mathbf{j}_k = \sum_{i=1}^{3} (j_{i,k} - j_{i,k-e_i}) = J \sum_{l \in NN(k)} (S_l^x S_k^y - S_l^y S_k^x) \tag{5.3}$$

which is just the negative right-hand side of Eq. (5.1). Note that the lattice spacing has been set to unity. In the spirit of hydrodynamics Eq. (5.1) can be interpreted as second order discretization of an equation of continuity of the form $\partial m_k / \partial t = -\nabla \cdot \mathbf{j}_k$. The density $m_k \equiv S_k^z$ and the current $\mathbf{j}_k$ defined by Eq. (5.2) are located on staggered meshes, i.e., the current density component $j_{i,k}$ associated with lattice site k is located half way between k and $k+e_i$, so that each of the finite differences appearing in Eq. (5.3) is located at lattice site k just as the left-hand side of Eq. (5.1). This displacement of spins and currents on the lattice has no further consequences in our case, because we have applied periodic boundary conditions in all lattice directions. According to Eq. (44) of Ref. 41 we find the expression

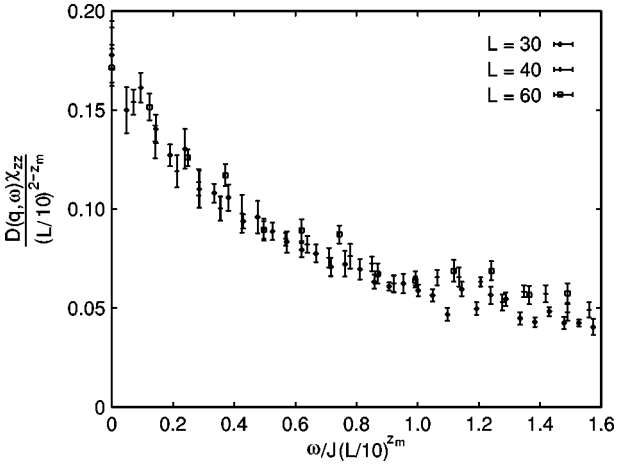

FIG. 14. Scaling plot of $D(q,\omega)\chi_{zz}/(L/10)^{2-z_m}$ versus $\omega/J(L/10)^{z_m}$ for $q=0$, $L=30$, 40, and 60, and $z_m=1.38$. The value $D(q=0,\omega=0)$ corresponds to the thermal conductivity.

$$D(q,\omega) = \frac{1}{k_B T \chi_{zz}} \frac{2}{\pi} \int_0^\infty dt \sum_i \langle j_{1,0}(0) j_{1,i}(t) \rangle \times \cos \mathbf{q} \cdot \mathbf{R}_i \cos \omega t \tag{5.4}$$

for the transport coefficient $D(q,\omega)$, where $\mathbf{q}=(q,0,0)$ and the same normalization as in Eq. (4.2) has been used. Note that the out-of-plane static susceptibility $\chi_{zz} = \langle M_z^2 \rangle / (k_B T L^3)$ needed for normalization in Eq. (5.4) is essentially constant as a function of system size L at fixed temperature. In the following we will analyze $D(q,\omega)$ only for $T=T_c$, where $\lambda \equiv D(0,0)$ corresponds to the thermal conductivity measured in ^{4}He experiments. According to Eq. (5.1) the current density $\mathbf{j}_k$ has the scaling dimension $1 - z_m - d/2$, because χ_{zz} has the scaling dimension zero. From Eq. (5.4) we then find $2(1-z_m-d/2)+d+z_m = 2 - z_m$ as the scaling dimension of $D(q,\omega)$ so that naive finite-size scaling yields $D(0,0)=\lambda \sim L^{2-z_m}$ at the critical point.[25] We therefore expect the scaling form

$$D(q,\omega) k_B T_c \chi_{zz} = L^{2-z_m} \Delta(qL, \omega L^{z_m}) \tag{5.5}$$

at $T=T_c$, where $k_B T_c \chi_{zz}$ is just a normalization factor. A corresponding scaling plot of $D(q,\omega)\chi_{zz}$ versus ω/JL^{z_m} for $L=30$, 40, and 60 and $q=0$ is shown in Fig. 14, where we have used our estimate $z_m=1.38$. The statistical noise in the data for $D(q,\omega)$ is considerably larger than the noise in the data for the structure factor (see also Ref. 40). The spread of the data points in Fig. 14 is of the same magnitude as the scatter of the data in each individual data set displayed. In view of these statistical uncertainties our data scale reasonably well for small ω and confirm the scaling exponent $2 - z_m \simeq 0.62$ [see Eq. (4.11)] of the transport coefficient $D(q,\omega)$. For $q \neq 0$ $D(q,\omega)$ scales accordingly as shown in Fig. 15 for $qL = 2\pi$. The position of the spin wave maximum appears to be shifted to the right as compared to the spin wave peak in $S_{zz}(q,\omega)$. According to Eq. (5.5) scaling is obtained up to a value of about 0.6 of the scaling argument for both $q=0$ and $qL=2\pi$. According to Fig. 15 the spin-wave maximum itself appears to be outside the scaling regime for the system sizes used here. For $q \neq 0$ $D(q,\omega)$ tends to zero as $\omega \to 0$ within the statistical errors.

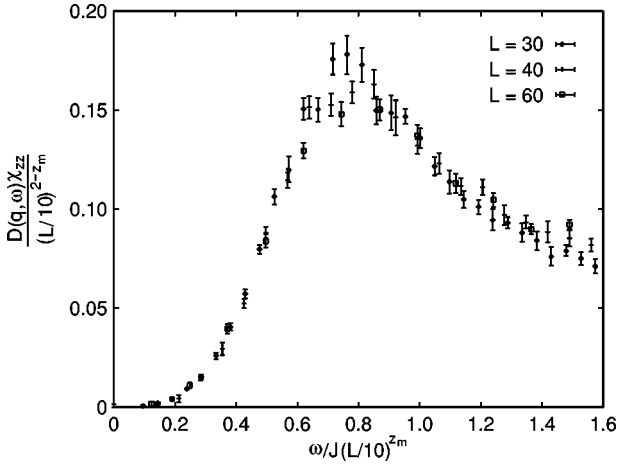

FIG. 15. Scaling plot of $D(q,\omega)\chi_{zz}/(L/10)^{2-z_m}$ versus $\omega/J(L/10)^{z_m}$ for $qL=2\pi$, $L=30$, 40, and 60, and $z_m=1.38$. $D(q,\omega)$ shows a strong spin wave resonance and it vanishes for $\omega\to 0$.

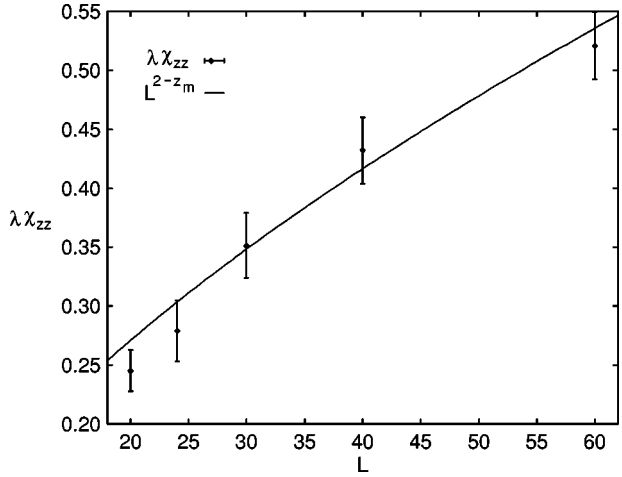

FIG. 16. Thermal conductivity $\lambda\chi_{zz}$ versus system size L for $L=20$, 24, 30, 40, and 60. The solid line displays the power law L^{2-z_m} for $z_m=1.38$ for comparison. The power law represents the data reasonably well for $L\geqslant 30$.

The thermal conductivity $\lambda=D(0,0)$ is shown in Fig. 16 as a function of the system size. The overall behavior of λ with L is captured quite well by the expected power law (full line) for $L\geqslant 30$ and even the data point for $L=24$ is only one standard deviation away. Systems with $L=20$ or less may be too small to be in the scaling regime. In view of the considerable statistical error in the data slowly varying corrections to scaling as discussed in the previous section cannot be identified. In any case more theoretical information is needed in order to provide a reliable background for the interpretation of spin dynamics data of transport coefficients in the critical regime.[38,39]

VI. SUMMARY AND CONCLUSIONS

The easy-plane Heisenberg ferromagnet belongs to the XY universality class which has been demonstrated by the evaluation of the critical exponents and the static structure factor. Unlike the standard plane rotator XY model the planar ferromagnet is endowed with a reversible spin dynamics which can be efficiently simulated by recently developed decomposition methods. Due to spatial and temporal symmetries the spin dynamics of the planar ferromagnet is expected to be in the same dynamic universality class as ^{4}He near the superfluid normal transition, but may have different corrections to scaling. The data have been compared to field-theoretic and mode-coupling predictions with the following main results.

(1) Above the critical regime the spin-dynamics data show a strong Lorentzian central peak in the in-plane component $S_{xx}(q,\omega)$ in agreement with mode coupling theory. The out-of-plane component $S_{zz}(q,\omega)$ displays a pseudo spin-wave peak which is also of Lorentzian shape and becomes increasingly prominent as q is increased. The presence of this peak is in accordance with field-theoretic predictions for $T>T_c$.

(2) Below the critical regime strong spin-wave peaks occur in both components of the dynamic structure factor. The shape of these peaks is captured very well by Lorentians as expected from mode-coupling theory. In addition to the spin-wave peak $S_{xx}(q,\omega)$ displays a central peak of Lorentzian shape and additional multi-spin-wave peaks which do not appear in $S_{zz}(q,\omega)$. For small q the dispersion relation $\omega(q)$ is linear in q and the linewidths $\Gamma_{xx}(q)$ and $\Gamma_{zz}(q)$ are quadratic in q as expected from mode-coupling theory. The qualitative agreement with the spin-dynamics data for $d=2$ suggests that the dynamics of the two-dimensional XY model may not be captured by vortex dynamics theories.

(3) At T_c, in contrast to mode-coupling theory and in agreement with field-theoretic predictions, $S_{xx}(q,\omega)$ and $S_{zz}(q,\omega)$ require different dynamic exponents in order to obtain scaling: $z_m=1.38\pm 0.05$ and $z_\phi=3-z_m=1.62\pm 0.05$, whereas mode coupling theory yields $z_m=z_\phi=3/2$. The out-of-plane component $S_{xx}(q,\omega)$ is dominated by a strong central peak. A shoulder at a finite frequency indicates the presence of a spin-wave signal. In $S_{zz}(q,\omega)$ a strong spin-wave peak remains the dominating feature. The line shapes are still compatible with Lorentzians, the central peak in S_{xx} is only compatible with a Gaussian shape very close to $\omega=0$.

(3) The transport coefficient $D(q,\omega)$, which provides access to the lattice analog of the thermal conductivity of ^{4}He within the XY model, has been investigated at T_c. The statistical fluctuations of the data are much stronger than those in the data for the structure factor which makes the scaling analysis less unique. However, scaling in agreement with the previously obtained dynamic exponents is obtained. The transport coefficient also shows a strong spin-wave resonance for finite q and vanishes for $\omega\to 0$ in this case. The thermal conductivity $\lambda=D(0,0)$ scales with the system size in the expected way within the error bars for sufficiently large systems.

ACKNOWLEDGMENTS

M. Krech gratefully acknowledges many helpful discussions with V. Dohm and financial support of this work through the Heisenberg program of the Deutsche Forschungsgemeinschaft. This research was supported in part by NSF Grant No. DMR - 9727714 and by the Computer Center of the RWTH Aachen.

[1] D.J. Amit, *Field Theory, the Renormalization Group, and Critical Phenomena* (McGraw-Hill, New York, 1978).
[2] G. Parisi, *Statistical Field Theory* (Addison-Wesley, Wokingham, 1988).
[3] P.C. Hohenberg and B.I. Halperin, Rev. Mod. Phys. **49**, 435 (1977).
[4] D.P. Landau and M. Krech, J. Phys.: Condens. Matter **11**, R179 (1999).
[5] K. Kawasaki, in *Phase Transitions and Critical Phenomena*, edited by C. Domb and M.S. Green (Academic, New York, 1976), Vol. 5a.
[6] E. Frey and F. Schwabl, Adv. Phys. **43**, 577 (1994).
[7] A. Keren, Phys. Rev. Lett. **72**, 3254 (1994).
[8] K. Chen and D.P. Landau, Phys. Rev. B **49**, 3266 (1994).
[9] A. Bunker, K. Chen, and D.P. Landau, Phys. Rev. B **54**, 9259 (1996).
[10] D.C. Rapaport and D.P. Landau, Phys. Rev. E **53**, 4696 (1996).
[11] K. Hirakawa and H. Yoshizawa, J. Phys. Soc. Jpn. **47**, 368 (1979).
[12] M.T. Hutchins, P. Day, E. Janke, and R. Pynn, J. Magn. Magn. Mater. **54**, 673 (1986).
[13] D.G. Wiesler, H. Zabel, and S.M. Shapiro, Z. Phys. B **93**, 277 (1994).
[14] J.M. Kosterlitz and D.J. Thouless, J. Phys. C **5**, L124 (1972); **6**, 1181 (1973).
[15] D.L. Huber, Phys. Rev. B **26**, 3758 (1982).
[16] F.G. Mertens, A.R. Bishop, G.M. Wysin, and C. Kawabata, Phys. Rev. Lett. **59**, 117 (1987); F.G. Mertens, A.R. Bishop, M.E. Gouvea, and G.M. Wysin, J. Phys. C **8**, 1385 (1988); F.G. Mertens, A.R. Bishop, G.M. Wysin, and C. Kawabata, Phys. Rev. B **39**, 591 (1989).
[17] M.E. Gouvea, G.M. Wysin, A.R. Bishop, and F.G. Mertens, Phys. Rev. B **39**, 11 840 (1989).
[18] A.R. Völkel, F.G. Mertens, A.R. Bishop, and G.M. Wysin, Phys. Rev. B **43**, 5992 (1991).
[19] D.P. Landau and R.W. Gerling, J. Magn. Magn. Mater. **104-107**, 246 (1992).
[20] H.G. Evertz and D.P. Landau, Phys. Rev. B **54**, 12 302 (1996).
[21] J.E.R. Costa and B.V. Costa, Phys. Rev. B **54**, 994 (1996); B.V. Costa, J.E.R. Costa, and D.P. Landau, J. Appl. Phys. **81**, 5746 (1997).
[22] S. Thoma, E. Frey, and F. Schwabl, Phys. Rev. B **43**, 5831 (1991).
[23] B.I. Halperin, P.C. Hohenberg, and E.D. Siggia, Phys. Rev. B **13**, 1299 (1976).
[24] C. De Dominicis and L. Peliti, Phys. Rev. B **18**, 353 (1978).
[25] V. Dohm, Z. Phys. B **33**, 79 (1978); V. Dohm and R.A. Ferrel, Phys. Lett. **67A**, 387 (1978).
[26] G. Ahlers, Phys. Rev. Lett. **21**, 1159 (1968); W.Y. Tam and G. Ahlers, Phys. Rev. B **32**, 5932 (1985).
[27] J.A. Lipa, D.R. Swanson, J.A. Nissen, T.C.P. Chui, and U.E. Israelsson, Phys. Rev. Lett. **76**, 944 (1996).
[28] V. Dohm, Phys. Rev. B **44**, 2697 (1991).
[29] U. Wolff, Phys. Rev. Lett. **62**, 361 (1989).
[30] M. Hasenbusch, Nucl. Phys. **B333**, 581 (1990).
[31] A.M. Ferrenberg, D.P. Landau, and Y.J. Wong, Phys. Rev. Lett. **69**, 3382 (1992); L.N. Shchur and H.W.J. Blöte, Phys. Rev. E **55**, R4905 (1997).
[32] A. M. Ferrenberg and D. P. Landau (unpublished).
[33] M. Krech, A. Bunker, and D.P. Landau, Comput. Phys. Commun. **111**, 1 (1998); J. Frank, W. Huang, and B. Leimkuhler, J. Comput. Phys. **133**, 160 (1997).
[34] K. Chen, A.M. Ferrenberg, and D.P. Landau, Phys. Rev. B **48**, 3249 (1993).
[35] A.P. Gottlob and M. Hasenbusch, Physica A **201**, 593 (1993).
[36] J.C. Le Guillou and J. Zinn-Justin, J. Phys. (France) Lett. **46**, L137 (1985); R. Guida and J. Zinn-Justin, J. Phys. A **31**, 8103 (1998).
[37] D.S. Ritchie and M.E. Fisher, Phys. Rev. B **5**, 2668 (1972).
[38] M. Töpler, Diplomarbeit, RWTH Aachen, Aachen, 1998.
[39] M. Krech, in *Computer Simulation Studies in Condensed Matter Physics XII*, edited by D.P. Landau, S.P. Lewis, and H.B. Schüttler (Springer-Verlag, Heidelberg, in press).
[40] N.A. Lurie, D.L. Huber, and M. Blume, Phys. Rev. B **9**, 2171 (1974).
[41] L.P. Kadanoff and P.C. Martin, Ann. Phys. (N.Y.) **24**, 419 (1963).